10-1-2023

Numerical study of flow characteristics around a 30° yawed circular cylinder at R e = 10 4

Ran Wang
University of Windsor

Shaohong Cheng
University of Windsor

David S.K. Ting
University of Windsor

Accepted to Phys. Fluids 10.1063/5.0172648

Numerical Study of Flow Characteristics Around a 30° Yawed Circular Cylinder at $Re = 10^4$

Ran Wang,[1] Shaohong Cheng,[1, a)] and David S-K. Ting[2]
[1)]*Department of Civil and Environmental Engineering, University of Windsor, Windsor, Ontario, N9B 3P4, Canada*
[2)]*Department of Mechanical, Automotive and Materials Engineering, University of Windsor, Windsor, Ontario, N9B 3P4, Canada*

(Dated: 29 September 2023)

Abstract

Unstable motions of bridge stay cables have been observed on site and in wind tunnel tests when a cable is yawed at certain orientations to wind. To uncover the underlying mechanisms, flow around a circular cylinder at a yaw angle of 30° has been numerically analyzed in the current study using delayed detached eddy simulation (DDES) at $Re = 10^4$. A comparison with the reference normal flow case indicates the presence of a more coherent span-wise flow structure when the cylinder is yawed at 30°. The application of Proper Orthogonal Decomposition (POD) further reveals that at this orientation, a synchronized flow structure exists which is characterized by continuous anti-symmetric pressure blocks. In addition, a low frequency flow fluctuation has been identified, the Strouhal number of which is roughly a quarter of that of the conventional Kármán vortex shedding. The pivotal role of axial flow in the intermittent amplification of cylinder sectional lift and the subsequent span-wise propagation of this enhanced local lift event has been revealed. The former is evident from the low frequency sectional lift peaks occurred during vortex shedding, whereas the propagation speed associated with the latter is in good agreement with the span-wise component of the incoming flow speed. The temporal and spatial impact of axial flow on the surrounding flow structure of the cylinder may serve as a periodic excitation source, which could trigger an unstable response of a cylinder. This, in the context of bridge stay cables, could possibly contribute to the onset mechanism of dry cable galloping.

[a)]Electronic mail: shaohong@uwindsor.ca

Accepted to Phys. Fluids 10.1063/5.0172648

INTRODUCTION

Due to low inherent damping, low lateral stiffness, and small mass, stay cables on cable-stayed bridges are prompt to wind excitation. Because of that, considerble amount of research effort has been made to understand the aerodynamics of stay cables. Majority of the existing analytical[1,2], experimental[3–5] and numerical[6] studies assumed stay cable as a smooth circular cylinder. In real life, however, stay cables are neither circular nor smooth. Furthermore, atmospheric wind tends to form a highly three-dimensional flow field around a stay cable, rendering unique aerodynamic forces depending on factors such as wind-cable orientation. Recently, a type of stay cable vibration characterized by low frequency and large amplitude has received special attention from the engineering community due to its potential threat to the safety of cable-stayed bridges. Among others, Saito *et al.*[7] conducted a dynamic test on a full-size stay cable model in a wind tunnel experiment. In a testing case where the cable was yawed at 45° and $Re = 7 \times 10^4$, the vibration amplitude of the inclined cable was tended to diverge. The relative angle between the cable axis and the oncoming flow is often used to describe the orientation of a stay cable. This angle is often referred to as the yaw angle or the angle of attack in literature, which is presumed to be a key factor in triggering unstable cable motion. Moreover, the unstable cable motion appeared to be difficult to restrain when wind speed exceeded a certain threshold. What is concerning is that the results from this study implied that majority of the existing stay cables on site would easily satisfy the identified critical condition and exhibit excessive oscillations. Though this new type of cable aerodynamic instability phenomenon has been studied for more than two decades, a consensus on its mechanism has yet to be reached.

Bursnall and Loftin[8] studied flow-induced surface pressure distribution of a circular cylinder over a yaw angle range of 0° to 60°, from the sub-critical Reynolds number range up to about 5.0×10^5. The observed pressure distribution on the cylinder surface showed some variations along its axial direction in the sub-critical Reynolds number range, indicating the presence of a highly three-dimensional flow structure. Further, it was noticed that this kind of surface pressure variation existed even in the normal flow case. They emphasized the importance of the axial flow effect on the cylinder surface pressure distribution.

King[9] experimentally visualized the flow pattern surrounding a stationary and an oscillating yawed circular cylinder for $2000 < Re < 20000$ in flowing water. They pointed out that yawing a cylinder would not necessarily protect the cylinder from vortex-excitation, but could enhance cylinder vibration at certain yaw angle positions. Zhou *et al.*[10] studied the fluid-structure interaction in the intermediate wake of a stationary circular cylinder. Based on the phase-averaging technique, they concluded that the three dimensionality of the wake was enhanced significantly by the span-wise flow. They found that the peak regions of the span-wise vorticity spectra were enlarged but the peak value of the energy was reduced, indicating a dispersion of the vortex shedding. It is worth noting that although the results obtained by Zhou *et al.*[10] indicated that vortex shedding was mitigated when the yaw angle was increased to 45°, King[9] reported that the vortex-induced vibration of an oscillating cylinder was enhanced at the same yaw angle. Chiba and Horikawa[11] calculated the viscoelastic fluid field around an inclined circular cylinder. They found that the fluid was prone to move axially in the vicinity of the cylinder and then gradually return to the direction of the oncoming flow.

Kawamura and Hayashi[12] computed incompressible three-dimensional flow around a finite and an infinite circular cylinder at a 30° yaw angle without considering turbulence effect when the Reynolds number was 2000. Axial flow was found to propagate downstream to the wake along the cylinder axis. Marshall[13] applied a quasi-two-dimensional approximation to study the wake dynamics of a yawed cylinder. The axial flow in the near wake of a yawed cylinder was found to have a speed 20% to 30% lower than that of the free-stream axial flow. They suspected that this axial velocity deficit within the downstream vortex cores might lead to instability of the vortex street. Zhao *et al.*[14] studied flow past a stationary yawed circular cylinder within a yaw angle range of 0° to 60° at $Re = 1000$ using direct numerical simulation. They observed that the span-wise vortices were parallel to the cylinder axis. Bourguet and Triantafyllou[15] calculated the response of a flexible cylinder inclined at 80° when $Re = 500$ by means of direct numerical simulation. They observed that in the absence of vibration, the wake behind the circular cylinder showed an oblique shedding mode.

The above studies showed that the relative angle between the oncoming flow and the cylinder axis had a decisive impact on the aerodynamic instability of a cylinder. In particular, a cylinder under certain angle of attack was found more prone to be excited and eventually develop into large amplitude unstable motion. For example, divergent response of a circular cylinder with an attack angle of 30° was observed in a wind tunnel study by Saito *et al.*[7] at $Re = 7 \times 10^4$. In another wind tunnel experiment by Cheng *et al.*[3], a cable segment model, when oriented with a relative angle of 30° between the cable axis and the oncoming flow, exhibited unstable galloping-like motion at $Re = 3.3 \times 10^5$. By conducting computational fluid dynamics (CFD) simulations at $Re = 10^4$, Wang *et al.*[16] identified a low-frequency but large amplitude sectional lift force at an attack angle of 30°. Yeo and Jones[17] investigated the 3D characteristic of flow around a yawed and inclined circular cylinder using detached eddy simulation (DES) at a Reynolds number of 1.4×10^5. They observed a coherent swirling flow structure developed from the separated shear layer. A unique moving peak of force, with a frequency lower than that of the conventional von Kármán vortex shedding, was generated as a result of the movement of these swirling flow structures at an attack angle of 22.2°. Due to the inherent three-dimensional characteristics of flow around a circular cylinder, locating the source of the low frequency force is arduous. A satisfactory explanation of how an attack angle would affect the aerodynamic response of a cylinder has yet to be reached.

CFD simulations provide abundant information related to the flow under investigation, including the ability to extract key characteristics from a statistical perspective. This method not only identifies coherent structures in the simulated flow but also serves as the foundation for constructing reduced-order models. The current study uses delayed detached eddy simulation (DDES) in Open-source Field Operation And Manipulation (OpenFOAM) to investigate the flow past a circular cylinder with a yaw angle of 30° at a Reynolds number of 10^4. Proper Orthogonal Decomposition (POD) analysis[18–20] is conducted for the surrounding flow to reveal the spatial and temporal flow characteristics. A normal flow case is also studied and used as a reference. The outcomes of the current study are expected to offer a deeper insight into the impact of cylinder orientation on the surrounding flow feature, helping to clarify mechanisms associated with wind-induced cable vibrations and contribute to the fundamentals of bluff body aerodynamics.

NUMERICAL ASPECTS

An O-type of grid is adopted in the current study. The computational grid has a cylindrical geometry. As shown in Fig. 1 (a), the cylinder is located at the centre of the computational domain, whose diameter and length are, respectively, $40D$ and $20D$, where D is the cylinder diameter. A Cartesian coordinate system is used such that the x-axis represents the stream-wise direction, the z-axis coincides with the cylinder axis, and the y-axis is perpendicular to both the x-axis and the z-axis. Fig. 1 (b) shows the definition of attack angle α. When $\alpha = 0^\circ$, it represents the normal flow condition. A total number of 4141200 hexahedral cells were used.

The following boundary conditions were used in the current study: a) At the inlet plane, a turbulent inlet was adopted, of which the corresponding turbulence intensity was around 1%; b) At the outlet plane, the pressure was assumed to be zero; c) On the cylinder surface, a no-slip boundary was applied for the velocity; and d) On the span-wise walls, the periodic boundary conditions were applied to minimize the end effect.

Detached eddy simulation (DES) is a hybrid model of Reynolds-averaged Navier-Stokes equation (RANS) and large eddy simulation (LES). DES assumes a destruction term and a production term such that it can adjust the eddy viscosity according to the relation between the distance to the closest wall and the size of the grid[21]. However, DES suffers from an artificial grid-induced separation if the switch mechanism from RANS to LES does not accurately reflect the flow properties within this transition region[22]. Due to this shortcoming, the delayed detached eddy simulation (DDES) was proposed to mitigate the weakness of the original DES[23]. Central to the DDES methodology is a set of equations that govern the transition from RANS to LES modes. The transition criterion is defined by the variable r_d :

$$r_\mathrm{d} \equiv \frac{\nu_t + \nu}{\sqrt{U_{i,j}U_{i,j}}\kappa^2 d^2} \tag{1}$$

Here, ν_t is the kinematic eddy viscosity, ν is the molecular viscosity, $U_{i,j}$ is the velocity gradients, κ is the von Kármán constant, and d is the distance to the nearest wall. Based on this criterion, the DDES shielding function f_d is formulated as:

$$f_\mathrm{d} \equiv 1 - \tanh\left([8r_\mathrm{d}]^3\right) \tag{2}$$

This function ensures a smooth transition between RANS and LES modes, preventing premature activation of LES in regions of attached boundary layers. It modifies the effective wall distance used in DES, enhancing the model's performance in areas with strong adverse pressure gradients. Lastly, a modified effective wall distance parameter d_{DDES} is introduced as:

$$d_{DDES} \equiv d - f_\mathrm{d}\max\left(0, d - C_\mathrm{DES}\Delta\right) \tag{3}$$

Here, C_DES is the DES constant and Δ is the grid spacing. These equations collectively constitute the mathematical foundation of the DDES method, enabling it to accurately capture a broad spectrum of turbulent flow regimes while maintaining computational efficiency.

The current study applies DDES with the finite volume method implemented in OpenFOAM[24] (version 4.1). The backward scheme was chosen for the time integration. The Pressure Implicit with Splitting of Operators algorithm was chosen to solve the discretized Navier-Stokes equations. At each time step, there were three loops to update

the pressure field after the momentum equations were solved using the pressure from the previous time step. The convergence criteria for solving the velocity and the pressure field were set to be 10^{-6} and 10^{-7}, respectively.

The numerical model was validated in terms of the mean drag coefficient and Strouhal number of a normal flow cylinder at $Re = 10^4$. The mean drag coefficient obtained from the current numerical model, observed to be 1.14, aligns reasonably well with the wall-resolved LES by Cheng et al.[25], which yielded $\overline{C_D} = 1.08$ at $Re = 10^4$. The Strouhal number, another critical validation metric, is also in line with the existing experimental data. Our numerical model produced a Strouhal number of $St = 0.20$ at the sub-critical Reynolds number of 10^4. This result exhibits close agreement with the experimental work of Roshko[26], which reported $St = 0.21$. Further, we observed in our analysis that the surface pressure distribution around the circular cylinder corresponded well with the experimental data presented by Norberg[27], as depicted in Fig. 2 by red dots. These results confirm the validity of our numerical model. The computational domain was established with a span-wise length of 20D. Details on the grid configuration can be found in Table I. Our previous studies show that the numerical solution was grid-independent with the current setups. For a deeper exploration of the validation process, please refer to our study[28]. Given that the normal flow scenario of the circular cylinder yields satisfactory results which are comparable with the existing experimental data and also manifest grid-independence, it validates the sufficiency of our numerical model, the meshing strategy, and the selected grid size for the simulation.

The fluctuating pressure $p'(x,t)$ is a function of the sampling location and time. POD can be used to approximate the original fluctuating pressure field using a spatial function $\mathbf{\Phi}_k(\mathbf{x})$ multiplied by time coefficients $a_k(t)$ such that:

$$\boldsymbol{p}'(\mathbf{x},t) = \sum_{k=1}^{\infty} a_k(t)\mathbf{\Phi}_k(\mathbf{x}), \tag{4}$$

where $\mathbf{\Phi}_k(\mathbf{x})$ $(k = 1, 2, ..., \infty)$ are the POD modes and $a_k(t)$ are the corresponding time coefficients.

Because it is challenging to prescribe physical meaning to higher order modes[29], the current study considered only the first six POD modes. According to Tamura and Suganuma[30], considering the mean value component in POD analysis of pressure field would be detrimental and could lead to a physical invalidity. Thus, the current POD analysis excluded the mean value component and focuses on the fluctuating components. A non-dimensional time is defined as $t^* \equiv tU_\infty/D$, where t is the dimensional time, U_∞ is the free-stream velocity, and D is the diameter of the cylinder. The number of time steps for POD analysis is chosen to be 1200, corresponding to 120 non-dimensional time duration. The reasons for choosing this time step are justified in the Appendix.

RESULTS AND DISCUSSION

To find out why the unstable aerodynamic behaviour of a circular cylinder is prone to occur at a yaw angle of 30°, flow structure surrounding a cylinder at this orientation will be explored in depth in this section by applying POD to the cylinder surface pressure and the transverse velocity of the flow in the near and far wake. In addition, the near wake vortical structures, the axial flow and the flow-induced forces will be scrutinized in

detail. The normal flow case ($\alpha = 0°$) will be used as a reference to reveal the impact of cylinder orientation on the surrounding flow and manifest the unique flow structure at an attack angle of 30°.

Surface pressure

Yawed cylinder case ($\alpha = 30°$)

Figure 3 shows the first six POD modes for the surface pressure in a yawed cylinder case at $\alpha = 30°$. A total number of 1200 snapshots of the instantaneous surface pressure data, all subtracted by the time-average surface pressure field, are used to conduct the POD analysis. The surface pressure POD modes are obtained by applying the single value decomposition to the time history of the fluctuating component of the surface pressure data. In each subplot, the horizontal axis represents the circumferential direction, θ. The stagnation point is located at $\theta = 180°$ or $\theta = -180°$. The base point is located at $\theta = 0°$. The vertical axis defines the dimensionless span-wise location. The pressure coefficient at each location is contoured and mapped by its magnitude. In general, the pressure modes show more variations in the region between $\theta = -130°$ and $\theta = 130°$, which corresponds to the wake region. The variations are largely driven by the alternating von Kármán vortex shedding that leads to periodic changes in the surface pressure distribution.

Modes 1 and 2 show an anti-symmetric pattern about the baseline $\theta = 0°$, which is related to von Kármán vortex shedding. The pressure/suction blocks in these two modes are observed to extend over the entire cylinder span. This means that localized von Kármán vortex shedding events are synchronized. While Mode 1 shows a very strong and well-coordinated von Kármán vortex shedding effect along the cylinder length, it is much weaker in Mode 2.

Modes 5 and 6 also exhibit an anti-symmetric pattern about the baseline, so they are related to von Kármán vortex shedding as well. More alternating pressure/suction blocks, two blocks for Mode 5 and three blocks for Mode 6, can be seen along the cylinder span. This clearly indicates the three-dimensionality of flow field around a yawed cylinder.

Modes 3 and 4 show a symmetric pattern about the baseline where these pressure/suction blocks cover the range of $-140° < \theta < 140°$. In Mode 3, the upper and lower parts of the cylinder are in high suction, whereas the mid-portion is subjected to high pressure. In Mode 4, the symmetric pattern can still be observed in the suction block of the upper part for $10 < Z/D < 18$, wherease the pressure block on the lower part of the cylinder loses the symmetry. The physical significance of these two modes is much more difficult to determine[29], but it could be the averaged flow that leads to pressurization on the windward side and suction on the leeward side.

Normal flow case ($\alpha = 0°$)

Figure 4 shows the first six POD modes for the surface pressure of the cylinder under the normal flow condition. Modes 1 and 2 show a clear anti-symmetric pattern about the baseline $\theta = 0°$. Unlike the 30° yaw angle case, when $\theta = 0°$, two pairs of pressure/suction blocks appear along the cylinder span in these two modes. The first pair is

seen to present in the top half of the cylinder, and the second pair in the bottom half with reversed sign. In addition, it is observed in Fig. 4 (a) that while strong pressure/suction exists in the upper part of the cylinder in Mode 1, they are much weaker in the lower half. Similar phenomenon can be seen in Fig. 4 (b) for Mode 2, except in this case, the upper part of the cylinder is subjected to weaker pressure/suction, and the lower half to stronger ones. Clearly, each pair of such pressure/suction blocks is associated with von Kármán vortex shedding, and the sign reversal between the upper and lower suggests that the formation and shedding of von Kármán vortices occur on the opposite sides and thus results in a three-dimensional flow field.

Modes 5 and 6 also exhibit an anti-symmetric pattern about the baseline $\theta = 0^\circ$. Compared to Modes 1 and 2, more pairs of alternating pressure/suction blocks are formed along the cylinder span for Mode 5 and 6, i.e. four pairs in Mode 5 and 3 pairs in Mode 6. This implies that numerous localized von Kármán vortex formation and shedding events with alternating shedding directions occurs along the cylinder span in these two modes which prompt the level of three-dimensionality in the surrounding flow.

Modes 3 and 4, however, show distinctively different mode shapes from the other modes. Both of them are symmetric about the baseline, so they are not related to von Kármán vortex shedding. In Mode 3, the upper ($15 < Z/D < 20$) and lower ($0 < Z/D < 8$) cylinder surface both show a high suction distribution over $-130^\circ < \theta < 130^\circ$, whereas the surface preesure in the cylinder mid-portion is nearly zero. In Mode 4, though the top ($16 < Z/D < 20$) and lower ($0 < Z/D < 7$) cylinder surface is still subjected to high suction, the presence of strong surface pressure is found when $10 < Z/D < 16$. All these three pressure/suction blocks extend from $\theta = -130^\circ$ to $\theta = 130^\circ$. Again, these two modes might be the averaged flow that leads to pressurization on the windward side and suction on the leeward side.

Surrounding flow structure

Near-wake vortical structures

Figure 5 shows the instantaneous vortex structures using iso-surface contour of the second invariant, Q[31]. The Q-criterion defines the vortex in an area where the vorticity magnitude is greater than the rate of strain. When $Q > 0$, it signifies there is a vortex. The presence of the primary and the secondary vortical structures can be clearly observed in Fig. 5. The former can be identified by the vortex tubes denoted by the red dash lines in the figure, whereas the latter appear as rib-like structures in between the primary vortical structures denoted by the green elliptical rings. These two types of vortical structures can be observed in both 30° and 0° cases.

As can be seen from the pattern of the red dash lines in Figs. 5 (a) and (b), the vortex tubes in both attack angle cases are parallel to each other. However, a noticeable difference in the primary vortical structure is the shape of the vortex tubes along the cylinder axial direction. In the case of $\alpha = 30^\circ$, the vortex tubes are parallel to the cylinder axis. However, this is not the case when the cylinder is normal to the flow. Since these vortex tubes represent the von Kármán vortices, their shape would show the state of von Kármán vortex shedding process at different span-wise locations. In the case of $\alpha = 30^\circ$, the vortex formation and shedding are synchronized along the cylinder span. In the time instant shown in Fig. 5 (a), there are three vortex tubes. The vortex tube labelled as L1 is

resulted from the newest von Kármán vortex that is shed, whereas L2 and L3 are formed in the two previous von Kármán vortex shedding events. In the normal flow case, four vortex tubes are captured at the shown time instant, as can be seen in Fig. 5 (b). For the most recent von Kármán vortex shedding event denoted by L1, a time lag between the two local von Kármán vortex shedding events at span-wise locations A1 and A2 can be clearly observed in Fig. 5 (b). At A1, the vortex tube is closer to the cylinder leeward surface than that at A2. This means that the vortex formation and shedding at A1 occurs later than that at A2. Thus, at the time instant when von Kármán vortex shed at location A1, the vortex formation and shedding at location A2 occurs on the opposite side of the cylinder. In other words, the shape of the four vortex tubes in the normal flow case suggests that at a given time instant, von Kármán vortex shedding and formation in the upper and lower part of the cylinder occurs on the opposite side of the cylinder.

POD of transverse velocity in wake region of $0.5 < x/D < 10$

Figure 6 shows the iso-surfaces of transverse velocity POD modes for $\alpha = 30^\circ$ and $\alpha = 0^\circ$. These modes were computed from the transverse velocity with a magnitude of ± 1 m/s in the wake region where $0.5 < x/D < 10$. For each snapshot, the time-average transverse velocity field is subtracted. The The approach of obtaining the wake transverse velocity POD modes is similar to that for the pressure POD modes except that the former is in a three-dimensional space. The red contour corresponds to 1 m/s, whereas the blue color represents -1 m/s.

In the column of $\alpha = 30^\circ$ case in Fig. 6, all tube-like structures are parallel to each other and continuous over the entire cylinder span in Mode 1 and Mode 2, except the tubes in Mode 2 are advanced in the streamwise direction by roughly 1D compared to their respective counterparts in Mode 1. Modes 1 and 2 represent a well-coordinated von Kármán vortex shedding process along the entire cylinder span. Since POD modes give an averaged value of the transverse velocity, the shape of Mode 1 and Mode 2 physically means that at any specific time instant, the formation and shedding of von Kármán vortices along the cylinder always occur on the same side of the cylinder. This is consistent with the earlier discussion of the surface pressure POD results of the $\alpha = 30^\circ$ case shown in Fig. 3 (a), where Mode 1 shows a uniform distribution pattern of the surface pressure and suction along the cylinder span on two opposite sides of the cylinder, implying the synchronization of the local von Kármán vortex shedding events along the cylinder.

Modes 3, 4, 5 and 6 have a similar feature in that the tube structures are divided into two or three segments along the cylinder span, with a streamwise lag between two adjacent segments, indicating that the occurence of von Kármán vortex shedding events on these two segments are on the opposite side of the cylinder. Therefore, these modes represent a strong 3D characteristic of the wake region. As discussed in Figs. 3 (e) and (f), the anti-symmetric pressure modes (Mode 5 and Mode 6) likewise show two or three pairs of reversed pressure/suction blocks along the cylinder spanwise direction.

For the normal flow case ($\alpha = 0^\circ$) shown in Fig. 6, the contour of the transverse velocity exhibits a tube-like structure in the wake. Modes 1 and 2 have the same spatial structure, except for a difference of roughly $1D$ in the tube position along the streamwise direction. In these two modes, all tube-like structures are found to be parallel to each other. However, unlike Mode 1 and Mode 2 in the $\alpha = 30^\circ$ case, when $\alpha = 0^\circ$, the tubes are seen to be divided into two parts, with those in the lower half region being

advanced by approximately $4D$ in the streamwise direction. This indicates that the vortex formation and shedding events are not synchronized along the cylinder, but rather they occur on the opposite sides of the cylinder in the upper and lower portions. As discussed earlier, the POD analysis of the cylinder surface pressure shows that Mode 1 and Mode 2 share similar spatial structures, as can be seen in Figs. 4 (a) and (b). These suggest that compared to the 30° yaw angle case, the coherence of von Kármán vortex shedding events along the cylinder axis exists in a much narrower region in the normal flow condition.

Each tube structure in Mode 3 is divided into three segments, covering a span-wise range of $14 < Z/D \leq 20$, $7 < Z/D \leq 14$, and $0 \leq Z/D \leq 7$, respectively. The top and the bottom tube segments are located roughly at the same streamwise position, whereas the middle segment is advanced by about $0.5D$, implying that at a specific time instant, the formation and shedding of von Kármán vortices occur on the same cylinder side at the top and bottom of the cylinder, whereas that in the middle part of the cylinder is not synchronized. Such an example can also be seen in Fig. 5 (b) where the vortex tube is farther away from the cylinder at A2 than that at A1. Mode 4 manifests the same spatial features as Mode 3. The main difference between these two modes is the sequence of the red and blue tubes in the stream-wise direction, which represents the presence of a phase shift between these two modes.

Modes 5 and 6 are similar to Modes 3 and 4, except some discontinuities in the tube structures at certain span-wise locations are observed. For example, in the zoom-in figure of Mode 5, a green circle highlights this kind of discontinuity which occurs at $z/D = 7$. In addition, Mode 6 shows a weaker von Kármán process in the upper wake region. Overall, Modes 3 to 6 in the normal flow case all represent the three-dimensional flow structures in the cylinder wake.

POD of transverse velocity in near wake ($0.5 < x/D < 1.5$)

The analysis of the transverse velocity in the near wake is a crucial element in understanding the aerodynamic subtleties of a cylinder. Alterations in this velocity component can reveal key fluid flow attributes, particularly those that trigger instability and generate large amplitude motions under specific conditions. These fluctuations can be linked directly to distinctive flow patterns and vortex structures, thereby enhancing our understanding of the complex aerodynamics. Subsequent sections focus on a detailed POD analysis of this specific flow region, 0.5D to 1.5D away from the cylinder, when the cylinder is at $\alpha = 30°$.

The transverse velocity POD analysis results, as depicted in Fig. 7, show the mode shapes and time coefficients. The dominance of von Kármán vortex is evident from the Fast Fourier Transform (FFT) results in Fig. 7 (a). It's worth noting that the POD analysis is unable to completely isolate von Kármán vortex, but instead display it across almost all of the modes. Nevertheless, the FFT analysis on the POD time coefficients of modes 5 and 6 show a noticeable difference in the pattern from that of the other four modes. Besides a peak at or in the vincity of $St = 0.20$ which reflects the effect of von Kármán vortex shedding, a low frequency peak, slightly broad-banded and approximately centered at $St = 0.12$, is observed.

Figures 7 (b) to (d) display the shape of Mode 5, which consists of four blocks. Considering the spatial distribution of this mode shape is repetitive in the z-direction, and factoring in the fluctuating nature of the time coefficient, it appears that a coherent struc-

ture is propagating in the z-direction. This information allows for the calculation of the propagation speed. On average, the length of each block is 0.45 m. The FFT results from Mode 5, as shown in Fig. 7 (a), indicate a slightly broad-banded frequency centered at $St = 0.1156$. With a normal velocity of 1.44 m/s and a cable diameter of 0.09 m, this calculation yields a dimensional frequency of $f = St \times U/D = 1.85$ Hz, which corresponds to a time period of 0.54 seconds. This leads to an observed propagation velocity of 0.83 m/s along the cylinder's span. It is important to note that under conditions of $Re = 10^4$ and $\alpha = 30^\circ$ for a circular object with a diameter of 0.09 m, the axial component of the free-stream velocity is determined to be 0.83 m/s, implying that the span-wise propagation of the observed coherent structure is highly associated with the axial flow formed on the leeward side of the cylinder.

Sectional resultant forces and wake

To further explore the flow structure associated with $\alpha = 30^\circ$ and $\alpha = 0^\circ$ cases, the shear layers at six different span-wise locations of $1.11D$, $4.44D$, $7.78D$, $11.11D$, $14.44D$, and $17.78D$ are portrayed in Fig. 8 for five representative time instants within one von Kármán vortex shedding period. These sections are denoted by a, b, c, d, e and f for referencing purpose. The shear layers in the figure are contoured using the vorticity component perpendicular to the selected section. In addition, the associated sectional resultant forces are also shown in these plots in blue. They are calculated from the integration of the surface pressure. The resultant forces are scaled by a factor of 5 for better visibility. For referencing purpose, a stream-wise center plane is defined by the cylinder axis and the stagnation point, which is shown as grey rectangles in Fig. 8, assuming readers face the stream-wise direction.

For the 30° attack angle case, at each of the five selected time instants, the sectional resultant forces at all six span-wise locations are found to point more or less toward the same direction, especially at $T^* = 674.74$, 679.54, and 680.54, implying that at a yaw angle of 30°, the resultant flow-induced force at different span-wise locations would "push" the cylinder towards the same direction, which would potentially lead to a large amplitude cylinder motion. On the other hand, the synchronization of sectional resultant forces is only observed over part of the cylinder in the normal flow case, i.e., the effect of the sectional resultant forces on different portions of the cylinder is partially cancelled out. Thus, the overall impact of the flow-induced forces on a normal flow cylinder is much less significant as compared to the 30° attack angle case.

Effect of axial flow

The orientation of a yawed cylinder renders the formation of a secondary flow structure along its span, which could have a sizable impact on the neighboring flow and the cylinder response. In this section, the influence of axial flow on the temporal and spatial variation of cylinder sectional lift will be examined. 3D flow visualization techniques will be used to acquire a better understanding of the flow characteristics in the near wake.

Impact on Temporal Variation of Sectional Lift To gain insights into the temporal variation of the sectional lift along the cylinder span, the sectional lift coefficient (C_L) at 100 equally-spaced span-wise locations are analyzed. Figure 9 (a) portrays a sample lift co-

efficient of Section 60 ($z = 12D$), the periodic variation of which is attributed to the shedding of von Kármán vortices. Besides, the existence of a low-frequency variation of C_L is also observed in Fig. 9 (a), such that the sectional lift is enhanced once ever few von Kármán vortex shedding cycles. A red envelope curve for C_L time history is added in Fig. 9 (a) to better encapsulate this kind of low frequency variation.

These observed features are further confirmed by the FFT analysis results, which revealed the presence of two dominant peaks in the frequency domain. The first peak occurs at a Strouhal number (St) of 0.20 and is associated with the frequency of von Kármán vortex shedding. The second peak is sligthly broad-banded and centered near $St = 0.05$, reflecting the low-frequency variation observed in the C_L time history plot. It is worth noting that the POD analysis of transverse velocity in the cylinder near wake reveals the existence of secondary axial flow characterized by approximately $St = 0.05$, as shown in Fig. in 7 (a) for mode 5 and mode 6. The matching low-frequency component in the transverse velocity of the near wake and the intermittent amplification of sectional lift suggest that the secondary axial flow could be the cause of the intermittent enhancement of C_L. The sectional lift time history and the corresponding FFT analysis results have been examined for the rest 99 span-wise sections. The same two dominant peaks in C_L have been identified. The consistency of the results support our understanding of the role of axial flow in affecting temporal variation of cylinder sectional lift.

Impact on Spatial Variation of Sectional Lift To examine the spatial variation of sectional lift, the C_L time history at Sections 43, 50, 68, 70, and 78, spanning from $8.6D$ to $15.6D$ along axial direction of the cylinder, are presented together in Fig. 10 for comparison. In the figure, the intermittent amplification events of sectional lift, encapsulated by C_L envelopes, are marked with black elliptical rings. These events are observed to propagate along the span of the cylinder. Three such propagation events have been identified within the timeframe shown in Fig. 10. They are designated by the purple, green, and blue lines, respectively.

Events T_f and T_g on the blue line are used as an example to illustrate how the propagation speed of these lift amplification events was calculated. The distance between Section 43 and 50 is 0.112m. The time lag between events T_f at Section 43 to event T_g at Section 50 is 0.14s. The propagation speed is then calculated as $0.112\ \text{m}/0.14\ \text{s} = 0.80\ \text{m/s}$. The same calculation was extended to all nine identified lift amplification events identified in Fig. 10. The average propagation speed was found to be 0.80 m/s and listed in Table II, which is very close to the axial component of the free-stream velocity, 0.83 m/s. This consistency implies that the span-wise propogration of the amplified sectional lift event is also caused by the effect of axial flow.

The above observations of the temporial and spatial varying characteristics of cylinder sectional lift reveal the pivotal role of the secondary axial flow in causing the intermittent amplification of sectional lift and their propagation along the cylinder span, both resulted from the interaction between von Kármán vortex and axial flow.

Visualization of Flow Characteristics Flow visualization is an integral technique for interpreting complex flow fields. In this study, a stream-trace visualization technique is utilized to gain deeper insight into the flow characteristics in the near wake. Figure 11 illustrates the flow around a circular cylinder at $\alpha = 30^\circ$ and $\alpha = 0^\circ$. Two types of stream-traces, red and black, are used. The red stream-traces, originating from the inlet boundary, assist in capturing the primary flow features, while the black stream-traces, stemming from the cylinder surface, trace the flow close to the cylinder leeward surface,

providing insights into the secondary axial flow dynamics.

As shown in Fig. 11, upon reaching and passing the cylinder at any given span-wise location, a fraction of the flow is entrapped in the recirculation zone, which subsequently treaded along the cylinder. The aggregation of such entrapped flow across all span-wise locations gives rise to what is often termed as the "axial flow" in literature[4]. The axial flow exerts a "pushing" influence on flow close to the leeward side of the cylinder surface and those near wake, causing them to move along the cylinder span.

However, the axial flow is not stable and will "escape" from the recirculation zone via periodic axial vortex formation and shedding into the wake. The formation and shedding of axial vortices have an impact on the existing flow structure, including the conventional von Kármán vortices. If the formation and shedding of axial vortex occurs concurrently with von Kármán vortex an enlarged von Kármán vortex would be formed and shed, leading to an amplification of sectional lift.

Figure 12 demonstrates the interaction between the axial and von Kármán vortices. Massless particles are injected into the near wake and tracked by a red tube. Section 72 ($z/D = 14.44$) and Section 83 ($z/D = 16.67$) are selected to illustrate the surrounding flow structure. The contour represents the vorticity magnitude perpendicular to the free-stream velocity. At time $t^* = 754.96$, as shown in Fig. 12 (a), the particle is moving in the region close to Section 72. At the red region, marked by a black arrow Va, a vortex is forming. Moving to the time instance $t^* = 757.77$, as depicted in Fig. 12 (b), the massless particle is moving towards Section 83. Simultaneously, a relatively large vortical structure, marked by a black arrow Vb, begins to emerge, creating a low-pressure zone, which draws the particle toward. When the axial flow moves into the core of the von Kármán vortex and interacts with it, it creates a significantly larger vortex. This particle is eventually shed into the far wake, indicated by the time instance $t^* = 759.77$ as shown in Fig. 12 (c).

Given the frequency of axial vortex formation and shedding is a fraction of the von Kármán vortex frequency, the sectional lift is amplified intermittently. Under the current simulation conditions, the axial vortex sheds approximately once every four von Kármán vortex sheddings, as illustrated with the help of Fig. 9 (b). This intermittent amplification of sectional lift, if persists and occurrs at different span-wise locations, could possibly become an excitation source to trigger unstable cylinder response. This, in the context of bridge stay cables, could potentially contribute to the onsite mechanism of a dry cable galloping. In a recent wind tunnel study[32], the dynamic response of stay cable in dry condition was examined. Results showed that at lower wind speeds, von Kármán vortices were mainly linked to minor vibrations. As wind speed increased, the impact of von Kármán vortices decreased, whereas low-frequency vortices became more prevalent, thereby enhancing the cable vibrations. The current findings regarding the mingling of axial flow with von Kármán vortices, leading to the shedding of larger, as presumably stronger, vortices shedding at lower than von Kármán frequency, offer an intriguing avenue for further exploration and validation in future research.

CONCLUSION

Flow around a circular cylinder yawed at 30° has been numerically studied by conducting delayed detached eddy simulation and compared with that around a normal flow cylinder. POD analysis has been performed to the cylinder surface pressure and

wake flow transverse velocity. The near wake vortical structures have been identified using instantaneous iso-surface contour of Q. In addition, the stream-trace flow visualization technique has been applied to assist in revealing flow characteristics in the near wake. The axial flow, which is a secondary flow formed by the entrapped flow in the recirculation zone, has been extensively analyzed in this study. The unique features of the flow around a cylinder yawed at $\alpha = 30^\circ$ have been scrutinized. The main findings of the current study are summarized as follows:

- A low-frequency flow structure in a cylinder oriented at a yawed angle of 30° has been identified. This structure, with a slightly broad-banded frequency range centered around St = 0.05, differs from classical von Kármán vortex shedding patterns. Confirmation of the existence of this structure through Proper Orthogonal Decomposition (POD), time history of sectional lift, and stream-trace visualization deepens our understanding of the complex flow dynamics involved.

- The presence of axial flow has been captured on the leeward side of a cylinder when it is yawed at 30°. This disturbs the local von Kármán vortex structures and tends to "correct" the direction of the sectional resultant forces along the cylinder span, aligning them more or less towards the same direction. This could generate a greater overall effect to displace the cylinder from its neutral position. Such a harmony in the direction of sectional resultant forces is not observed in a normal flow cylinder without axial flow.

- For a cylinder yawed at 30°, it was observed that the axial flow tends to enhance the local lift and propagate this amplified event along the span, leading to an intermittent amplification of sectional lift. This could impose a periodical low frequency excitation on the cylinder, which, if sufficiently significant, could eventually lead to large amplitude unstable motion of the cylinder. This mechanism is believed to contribute to dry cable galloping of bridge stayed cables.

- Synchronized flow structures are observed at $\alpha = 30^\circ$. This is also characterized by the continuous anti-symmetric pressure blocks over the entire cylinder span as appeared in the surface pressure POD mode shapes, and the coordination of local von Kármán vortex shedding events along the cylinder span observed from the instantaneous iso-surface contour of Q. In contrast, such a flow structure coherence only exists within limited range along the cylinder span in the normal flow case.

- POD is capable of capturing the most cohesive spatial features in the flow around a cylinder. The POD mode shapes of the cylinder surface pressure show both anti-symmetric and symmetric patterns of pressure/suction blocks in the cylinder circumferential direction, of which the former is associated with the von Kármán vortex shedding and the latter could be the averaged flow that leads to pressurization of the windward side and suction on the leeward side. Besides, the complex three-dimensional flow field surrounding a circular cylinder is evidenced by the presence of multiple pressure/suction blocks along the cylinder span in the POD mode shapes.

- The temporal characteristics of the flow around a cylinder are captured by the POD mode shapes of the transverse velocity of the wake flow. Continuous tube struc-

tures in the first two modes of the 30° yawed cylinder represent the synchronization of local von Kármán vortex shedding along the span. The multi-segment tube structures observed in the remaining four modes of the 30° yawed cylinder and all six modes of the normal flow cylinder case suggest that there is a time lag in the shedding of local von Kármán vortices at different span-wise locations of the cylinder.

ACKNOWLEDGMENTS

This research was enabled in part by support provided Compute Canada. The authors are grateful to the Natural Sciences and Engineering Research Council of Canada (NSERC) for supporting this project.

AUTHOR DECLARATIONS

Conflict of Interest

The authors have no conflicts to disclose.

DATA AVAILABILITY

The data that support the findings of this study are available from the corresponding author upon reasonable request.

APPENDIX

Time sensitivity analysis

To ensure using the same time window in the analysis for the case $\alpha = 0°$, a time sensitivity analysis was conducted. The number of time instants used in the study are 1800, 1200 and 1000, respectively. The first six POD mode shapes of the cylinder surface pressure obtained by using these three different time sequences are contoured in Figs. 13, 14, and 15, respectively. A comparison between these three sets of results showed that the patterns of the pressure POD mode shapes yielded from 1200 and 1800 time instants agree well. Therefore, the number of time instants used in the current study was chosen to be 1200.

POD script validation

To validate the POD script, the span-wise vorticity is processed with the current POD code. Figure 16 shows a comparison between the current results with those in a recently published study by Janocha *et al.*[33], both at $Re = 100$.

As can be seen in Fig. 16 (a), three types of mode shapes are captured in the current study. Mode 1 and Mode 2 show the largest block structure in the near wake. Mode 3 and

Mode 4 show an anti-symmetric pattern of block structure about $y/D = 0$. The size of blocks in Mode 5 and Mode 6 are much smaller and they are symmetric about $y/D = 0$. All these distinctive patterns are in good agreement with the span-wise vorticity POD analysis results by Janocha *et al.*[33].

REFERENCES

[1]A. Raeesi, S. Cheng, and D. S.-K. Ting, "A two-degree-of-freedom aeroelastic model for the vibration of dry cylindrical body along unsteady air flow and its application to aerodynamic response of dry inclined cables," Journal of Wind Engineering and Industrial Aerodynamics **130**, 108–124 (2014).
[2]M. He and J. H. Macdonald, "An analytical solution for the galloping stability of a 3 degree-of-freedom system based on quasi-steady theory," Journal of Fluids and Structures **60**, 23–36 (2016).
[3]S. Cheng, G. L. Larose, M. G. Savage, H. Tanaka, and P. A. Irwin, "Experimental study on the wind-induced vibration of a dry inclined cable-Part I: Phenomena," Journal of Wind Engineering and Industrial Aerodynamics **96**, 2231–2253 (2008).
[4]M. Matsumoto, T. Yagi, H. Hatsuda, T. Shima, M. Tanaka, and H. Naito, "Dry galloping characteristics and its mechanism of inclined/yawed cables," Journal of Wind Engineering and Industrial Aerodynamics **98**, 317–327 (2010).
[5]W. Ma, Q. Liu, and M. Matsumoto, "Excitation of the large-amplitude vibrations of a circular cylinder under normal wind conditions in the critical reynolds number range," Journal of fluids and structures **84**, 318–328 (2019).
[6]D. Yeo and N. P. Jones, "A mechanism for large amplitude, wind-induced vibrations of stay cables," in *Proceedings of the Eleventh Americas Conference on Wind Engineering, San Juan, Puerto Rico* (2009).
[7]T. Saito, M. Matsumoto, and M. Kitazawa, "Rain-wind excitation of cables on cable-stayed Higashi-Kobe Bridge and cable vibration control," in *Proceedings of the International Conference on cable-stayed and suspension bridges (AFPC)*, Vol. 2 (1994) pp. 507–510.
[8]W. J. Bursnall and L. K. Loftin, "Experimental investigation of the pressure distribution about a yawed circular cylinder in the critical Reynolds number range," National Aeronautics and Space Administration , NACA-TN-24 (1951).
[9]R. King, "Vortex excited oscillations of yawed circular cylinders," Journal of Fluids Engineering **99**, 495–501 (1977).
[10]T. Zhou, H. Wang, S. F. Razali, Y. Zhou, and L. Cheng, "Three-dimensional vorticity measurements in the wake of a yawed circular cylinder," Physics of Fluids **22**, 10–15 (2010).
[11]K. Chiba and A. Horikawa, "Numerical solution for the flow of viscoelastic fluids around an inclined circular cylinder," Rheologica Acta **254**, 243–254 (1987).
[12]T. Kawamura and T. Hayashi, "Computation of flow around a yawed circular cylinder," JSME International Journal Series B Fluids and Thermal Engineering **37**, 229–236 (1994).
[13]J. S. Marshall, "Wake dynamics of a yawed cylinder," Journal of Fluids Engineering **125**, 97–103 (2003).
[14]M. Zhao, L. Cheng, and T. Zhou, "Direct numerical simulation of three-dimensional flow past a yawed circular cylinder of infinite length," Journal of Fluids and Structures **25**, 831–847 (2009).
[15]R. Bourguet and M. S. Triantafyllou, "The onset of vortex-induced vibrations of a flexible cylinder at large inclination angle," Journal of Fluid Mechanics **809**, 111–134 (2016).
[16]R. Wang, S. Cheng, and D. S.-K. Ting, "Effect of yaw angle on flow structure and cross-flow force around a circular cylinder," Physics of Fluids **31**, 014107 (2019).
[17]D. Yeo and N. P. Jones, "Investigation on 3-D characteristics of flow around a yawed and inclined circular cylinder," Journal of Wind Engineering and Industrial Aerodynamics

96, 1947–1960 (2008).
[18]Z. Feng and Q. Ye, "Turbulent boundary layer over porous media with wall-normal permeability," Physics of Fluids **35** (2023).
[19]K. V. Pham, A. D. Le, C.-T. Dinh, *et al.*, "Frequency characteristics of axisymmetric conical boattail models with different slant angles," Physics of Fluids **35** (2023).
[20]H. Li, R. Peng, L. Hu, X. He, and A. Kareem, "On the surface flow patterns and associated aerodynamics of an asymmetrical flat-box section," Physics of Fluids **35** (2023).
[21]P. R. Spalart, "Detached-eddy simulation," Annual review of fluid mechanics **41**, 181–202 (2009).
[22]F. R. Menter and M. Kuntz, "Adaptation of eddy-viscosity turbulence models to unsteady separated flow behind vehicles," in *The Aerodynamics of Heavy Vehicles: Trucks, Buses, and Trains*, The Aerodynamics of Heavy Vehicles: Trucks, Buses, and Trains (Springer Berlin Heidelberg, 2004) pp. 339–352.
[23]P. R. Spalart, S. Deck, M. L. Shur, K. D. Squires, M. K. Strelets, and A. Travin, "A new version of detached-eddy simulation, resistant to ambiguous grid densities," Theoretical and computational fluid dynamics **20**, 181 (2006).
[24]H. G. Weller, G. Tabor, H. Jasak, and C. Fureby, "A tensorial approach to computational continuum mechanics using object-oriented techniques," Computers in Physics **12**, 620–631 (1998).
[25]W. Cheng, D. I. Pullin, R. Samtaney, W. Zhang, and W. Gao, "Large-eddy simulation of flow over a cylinder with Re_D from 3.9×10^3 to 8.5×10^5 : a skin-friction perspective," Journal of Fluid Mechanics **820**, 121–158 (2017).
[26]A. Roshko, "On the development of turbulent wakes from vortex streets," NACA Technical Report 1191 (1954).
[27]C. Norberg, "Pressure forces on a circular cylinder in cross flow," in *IUTAM Symposium on Bluff Body Wakes, Dynamics and Instabilities*, edited by H. Eckelmann, J. M. R. Graham, P. Huerre, and P. A. Monkewitz (Springer Berlin Heidelberg, Berlin, Heidelberg, 1993) pp. 275–278.
[28]R. Wang, S. Cheng, and D. S.-K. Ting, "Numerical study of roundness effect on flow around a circular cylinder," Physics of Fluids **32**, 044106 (2020).
[29]Q. Zhang, Y. Liu, and S. Wang, "The identification of coherent structures using proper orthogonal decomposition and dynamic mode decomposition," Journal of Fluids and Structures **49**, 53–72 (2014).
[30]Y. Tamura, H. Ueda, H. Kikuchi, K. Hibi, S. Suganuma, and B. Bienkiewicz, "Proper orthogonal decomposition study of approach wind-building pressure correlation," Journal of Wind Engineering and Industrial Aerodynamics **72**, 421–431 (1997).
[31]J. C. R. Hunt, A. A. Wray, and P. Moin, "Eddies, streams, and convergence zones in turbulent flows," Center for Turbulence Research, Proceedings of the Summer Program , 193–208 (1988).
[32]D. T. Nguyen and D. H. Vo, "Further explanation on the excitation mechanism of stay cable vibration in dry conditions," Buildings **13**, 1543 (2023).
[33]M. J. Janocha, G. Yin, and M. C. Ong, "Modal analysis of wake behind stationary and vibrating cylinders," Journal of Offshore Mechanics and Arctic Engineering **143**, 041902 (2021).
[34]A. Travin, M. Shur, M. Strelets, and P. Spalart, "Detached-eddy simulations past a circular cylinder," Flow, Turbulence and Combustion **63**, 293–313 (1999).
[35]P. D. Weidman, "Wake transition and blockage effects on cylinder base pressures,"

662 Ph.D. thesis, California Institute of Technology (1968).
663 [36]S. Dong, G. E. Karniadakis, A. Ekmekci, and D. Rockwell, "A combined direct numer-
664 ical simulation-particle image velocimetry study of the turbulent near wake," Journal
665 of Fluid Mechanics **569**, 185–207 (2006).
666 [37]C. Norberg, "LDV-measurements in the near wake of a circular cylinder," ASME Paper
667 No. FEDSM98-521 (1998).

TABLES

TABLE I. Mesh information and validation data.

Case	Re	L_z/D	N_r $(\Delta r^+)^a$	N_θ $(\Delta\theta^+)$	N_z (Δz^+)	$\overline{C_D}$	S_t	C'_L	$-C_p$	$\lvert u_{\min}\rvert/U$	$\overline{L}_B/D$
Current	1.0×10^4	20	115	118	300	1.14	0.20	0.23	0.96	0.28	1.11
			0.004	0.026	0.067						
Cheng *et al.*[25]	1.0×10^4	3	384	384	96	1.08	…	…	1.20	…	…
Travin *et al.*[34]	5.0×10^4	2	118	105	30	1.05	0.22	0.21	0.98	…	1.3
Expt. Data	…	…	…	…	…	…	0.21[b]	…	1.10[c]	0.38[d]	1.02[e]

[a] The dimensionless thickness of the near-wall mesh, $\Delta r^+ = d/D$, where d is the dimensional thickness and D is the diameter of the cylinder.
[b] Ref.[26]
[c] Ref.[35]
[d] Ref.[36]
[e] Ref.[37]

TABLE II. Calculation of the average axial flow interaction velocity shown in Fig. 8. Three events are captured, and they are indicated by purple, green, and blue lines. The amplified sectional C_l are being circled with elliptical rings.

Line	Color	# sections	t_{end} (s)	t_{start} (s)	dt (s)	velocity (m/s)
Line 1	Purple	8	38.376	38.214	0.162	0.790
Line 2	Green	10	39.472	39.273	0.199	0.804
Line 2	Green	18	39.786	39.472	0.314	0.917
Line 3	Blue	7	39.305	39.165	0.140	0.800
Line 3	Blue	18	40.477	40.066	0.411	0.701
Line 3	Blue	10	40.677	40.477	0.200	0.800
						(Avg.) 0.802

Accepted to Phys. Fluids 10.1063/5.0172648

669 **FIGURE CAPTIONS**

FIG. 1. Schematic representation of the model: (a) sketch of full domain and (b) definition of attack angle α.

FIG. 2. Mean pressure distribution on cylinder surface at $Re = 10^4$ for the normal flow case (red rectangles are interpolated from Norberg's[27] experimental data). The red rectangles indicate the regions where our results closely align with Norberg's experimental data.

FIG. 3. The first six POD mode shapes for the surface pressure at $Re = 10^4$ and $\alpha = 30^\circ$: (a) Mode 1; (b) Mode 2; (c) Mode 3; (d) Mode 4; (e) Mode 5; and (f) Mode 6. Modes 1,5, and 6 exhibit anti-symmetric distributions, which are closely related to von Kármán vortex shedding.

FIG. 4. The first six POD mode shapes for the surface pressure at $Re = 10^4$ and $\alpha = 0^\circ$: (a) Mode 1; (b) Mode 2; (c) Mode 3; (d) Mode 4; (e) Mode 5; and (f) Mode 6. Much like the $\alpha = 30^\circ$ case, anti-symmetric distribution emerges as the most dominant pattern.

FIG. 5. Instantaneous iso-surface of Q = 50 s^{-2} showing the near wake vortorical structure at $Re = 10^4$: (a) $\alpha = 30^\circ$; and (b) $\alpha = 0^\circ$. The vortex tube in the $\alpha = 30^\circ$ scenario aligns more closely with the cylinder's centerline compared to the $\alpha = 0^\circ$ case.

FIG. 6. The first six POD mode shapes of transverse velocity in the cylinder wake region of $0.5 < x/D < 10$ in two cases: $\alpha = 30^\circ$; and $\alpha = 0^\circ$. Modes 1 and 2 show greater coherence along the cylinder's axis, suggesting more synchronized vortex shedding at $\alpha = 30^\circ$.

FIG. 7. POD analysis results on transverse velocity in the near wake region ($0.5 < x/D < 1.5$) of a cylinder at $\alpha = 30^\circ$ and $Re = 10^4$: (a) time coefficeints and their respective FFT resutls; (b) mode shape of M5, perspective view; (c) mode shape of M5, side view; (d) mode shape of M5, leeward-side view. POD analysis identifies secondary flow features propagating along the cylinder's axis.

FIG. 8. Visualization of cylinder wake and sectional resultant forces at $\alpha = 0^\circ$ and 30° when $Re = 10^4$. In the $\alpha = 30^\circ$ case, vortex shedding is more coherent along the cylinder's axis, resulting in a stronger overall resultant force.

FIG. 9. Sectional lift coefficient at section 60 (a) time history and (b) corresponding FFT analysis result. A secondary flow pattern is observed, exhibiting a frequency much lower than that at which von Kármán vortex sheds.

FIG. 10. Time history of sectional C_l with corresponding envelopes at six span-wise locations ($z = 0.817$ m, 0.933 m, 1.100 m, 1.233 m, 1.267 m, 1.400 m) displayed from top to bottom. The enhanced local lift events are marked out by black elliptical rings. The span-wise propagation of enhanced sectional lift appears to be influenced by axial flow effects.

FIG. 11. Axial flow visualization at $Re = 10^4$ for the cases: (a) $\alpha = 30^\circ$ and (b) $\alpha = 0^\circ$. Axial flow tends to move along the center axis and interact with von Kármán vortices, a feature not observed in the normal flow case.

FIG. 12. Visualization of the interaction between axial and von Kármán vortices with a massless particle tracked by a red tube. Three time instances demonstrate the particles' movement through planes, and the evolving vortical structure, leading to a larger von Kármán vortex that eventually pulls the particle into the far wake.

FIG. 13. The first six POD mode shapes for the surface pressure at $Re = 10^4$ and $\alpha = 0^\circ$. The number of time sequence is 1800.

FIG. 14. The first six POD mode shapes for the surface pressure at $Re = 10^4$ and $\alpha = 0^\circ$. The number of time sequence is 1200.

FIG. 15. The first six POD mode shapes for the surface pressure at $Re = 10^4$ and $\alpha = 0^\circ$. The number of time sequence is 1000.

FIG. 16. A comparison of the mode shape for the span-vise vorticity at $Re = 100$: (a) current POD result (b) result from Janocha *et al.*[33].

FIGURES

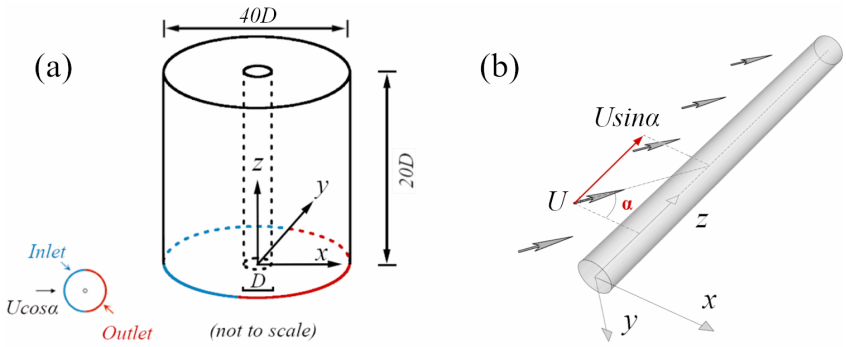

FIG. 1. Schematic representation of the model: (a) sketch of full domain and (b) definition of attack angle α.

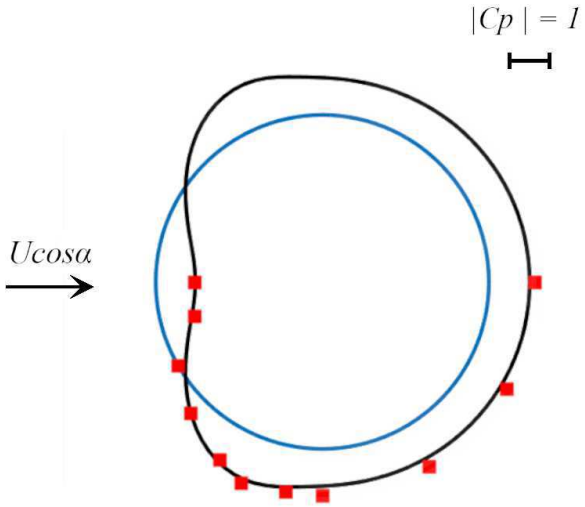

FIG. 2. Mean pressure distribution on cylinder surface at $Re = 10^4$ for the normal flow case (red rectangles are interpolated from Norberg's[27] experimental data). The red rectangles indicate the regions where our results closely align with Norberg's experimental data.

Accepted to Phys. Fluids 10.1063/5.0172648

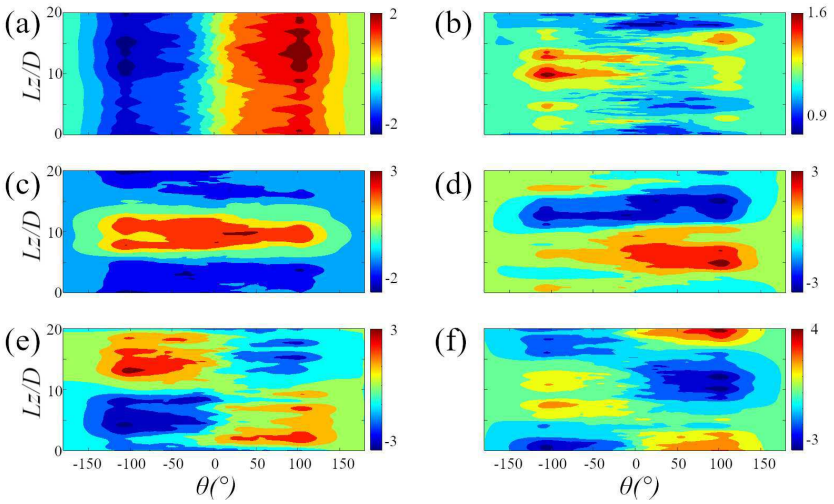

FIG. 3. The first six POD mode shapes for the surface pressure at $Re = 10^4$ and $\alpha = 30°$: (a) Mode 1; (b) Mode 2; (c) Mode 3; (d) Mode 4; (e) Mode 5; and (f) Mode 6. Modes 1,5, and 6 exhibit anti-symmetric distributions, which are closely related to von Kármán vortex shedding.

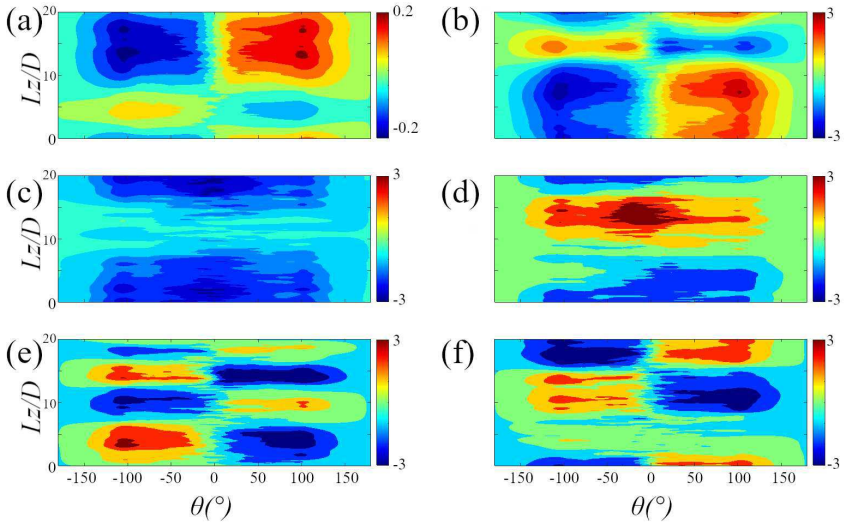

FIG. 4. The first six POD mode shapes for the surface pressure at $Re = 10^4$ and $\alpha = 0°$: (a) Mode 1; (b) Mode 2; (c) Mode 3; (d) Mode 4; (e) Mode 5; and (f) Mode 6. Much like the $\alpha = 30°$ case, anti-symmetric distribution emerges as the most dominant pattern.

Accepted to Phys. Fluids 10.1063/5.0172648

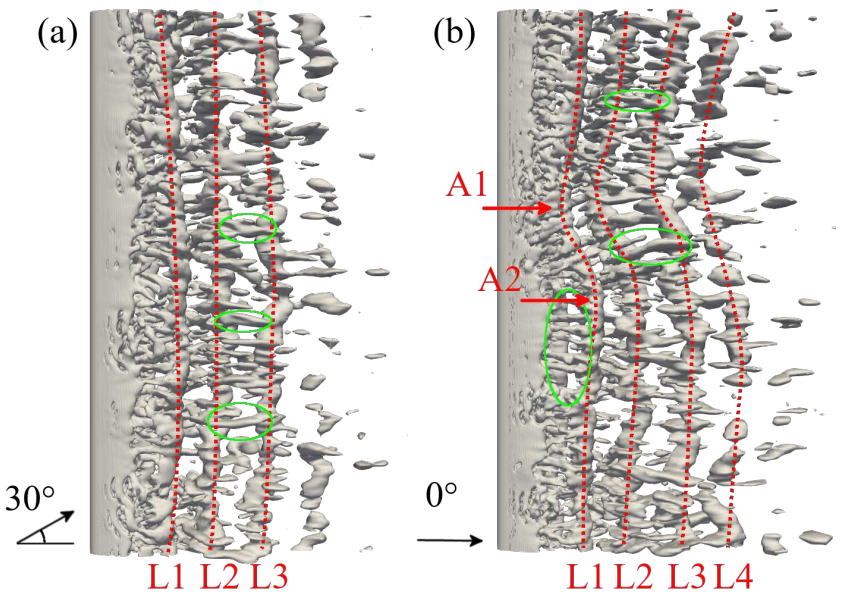

FIG. 5. Instantaneous iso-surface of Q = 50 s^{-2} showing the near wake vortorical structure at $Re = 10^4$: (a) $\alpha = 30°$; and (b) $\alpha = 0°$. The vortex tube in the $\alpha = 30°$ scenario aligns more closely with the cylinder's centerline compared to the $\alpha = 0°$ case.

Accepted to Phys. Fluids 10.1063/5.0172648

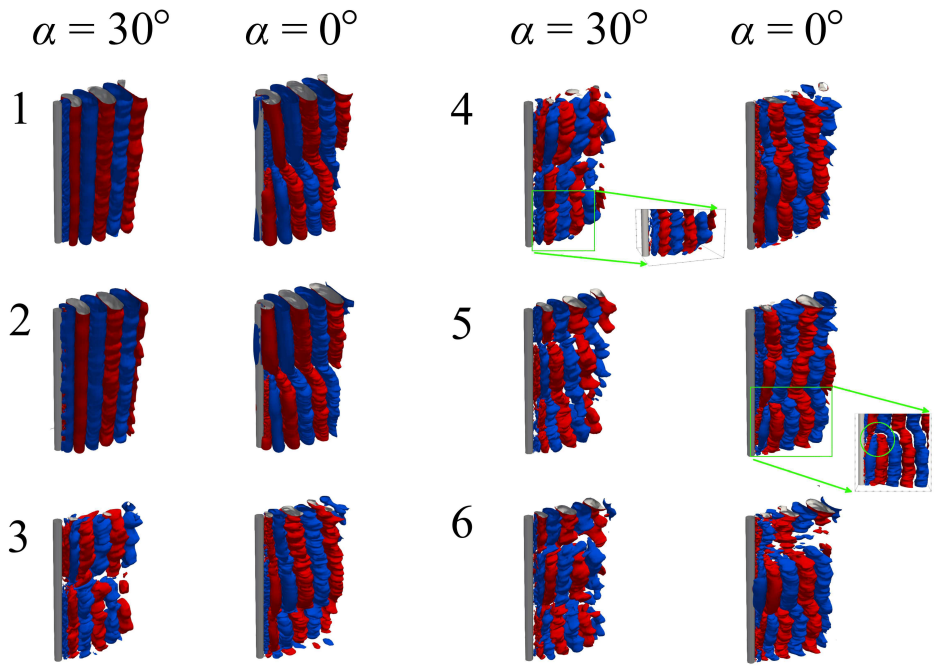

FIG. 6. The first six POD mode shapes of transverse velocity in the cylinder wake region of $0.5 < x/D < 10$ in two cases: $\alpha = 30°$; and $\alpha = 0°$. Modes 1 and 2 show greater coherence along the cylinder's axis, suggesting more synchronized vortex shedding at $\alpha = 30°$.

Accepted to Phys. Fluids 10.1063/5.0172648

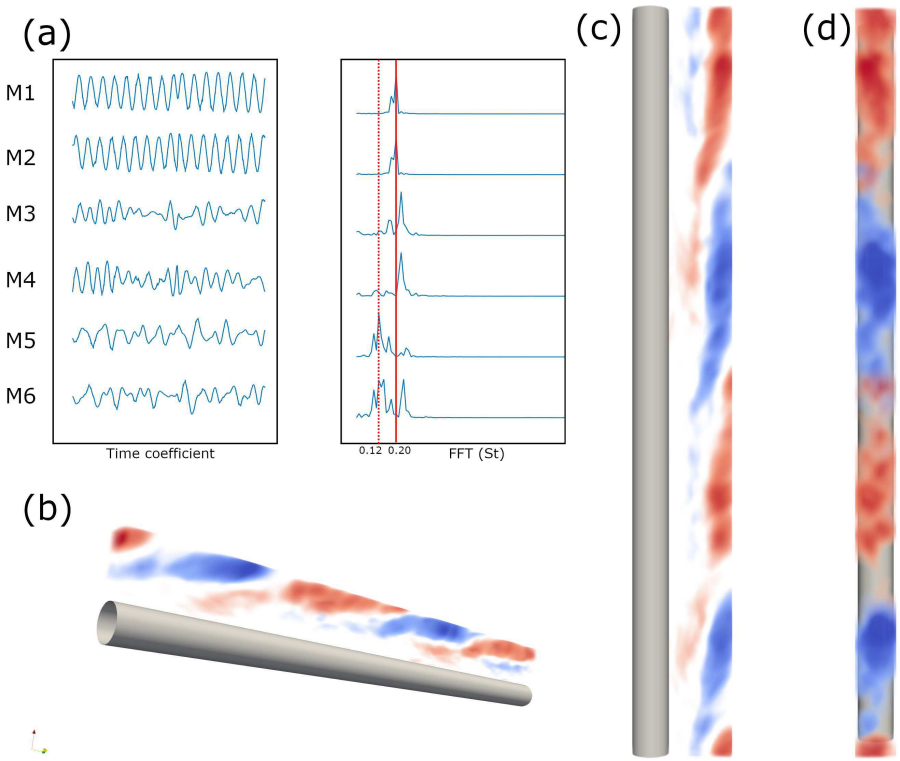

FIG. 7. POD analysis results on transverse velocity in the near wake region ($0.5 < x/D < 1.5$) of a cylinder at $\alpha = 30°$ and $Re = 10^4$: (a) time coefficeints and their respective FFT resutls; (b) mode shape of M5, perspective view; (c) mode shape of M5, side view; (d) mode shape of M5, leeward-side view. POD analysis identifies secondary flow features propagating along the cylinder's axis.

Accepted to Phys. Fluids 10.1063/5.0172648

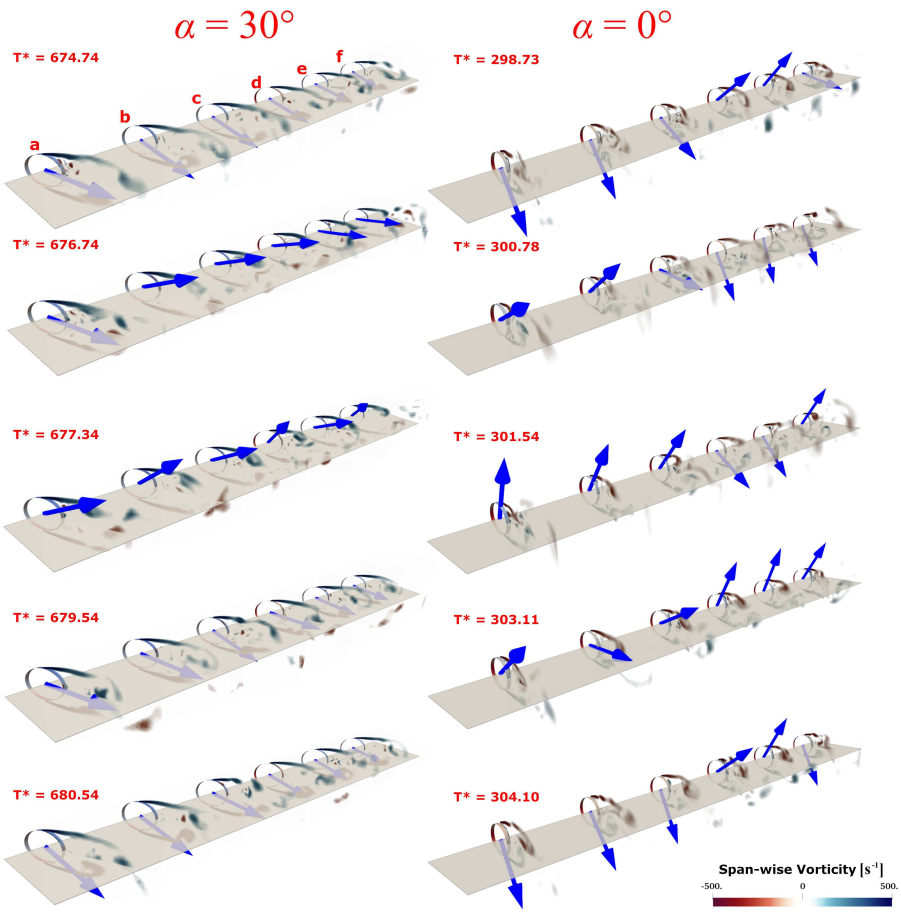

FIG. 8. Visualization of cylinder wake and sectional resultant forces at $\alpha = 0°$ and $30°$ when $Re = 10^4$. In the $\alpha = 30°$ case, vortex shedding is more coherent along the cylinder's axis, resulting in a stronger overall resultant force.

Accepted to Phys. Fluids 10.1063/5.0172648

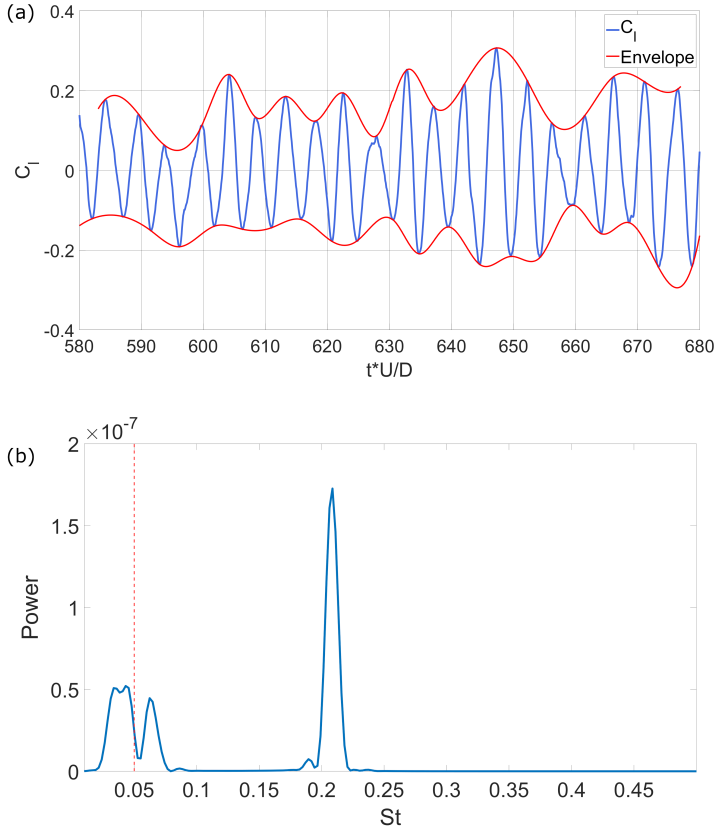

FIG. 9. Sectional lift coefficient at section 60 (a) time history and (b) corresponding FFT analysis result. A secondary flow pattern is observed, exhibiting a frequency much lower than that at which von Kármán vortex sheds.

Accepted to Phys. Fluids 10.1063/5.0172648

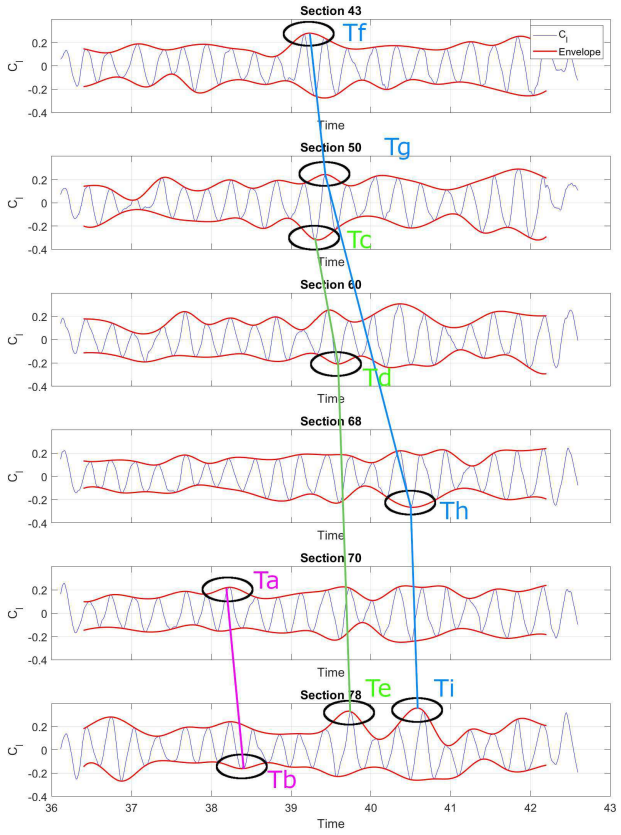

FIG. 10. Time history of sectional C_l with corresponding envelopes at six span-wise locations ($z =$ 0.817 m, 0.933 m, 1.100 m, 1.233 m, 1.267 m, 1.400 m) displayed from top to bottom. The enhanced local lift events are marked out by black elliptical rings. The span-wise propagation of enhanced sectional lift appears to be influenced by axial flow effects.

Accepted to Phys. Fluids 10.1063/5.0172648

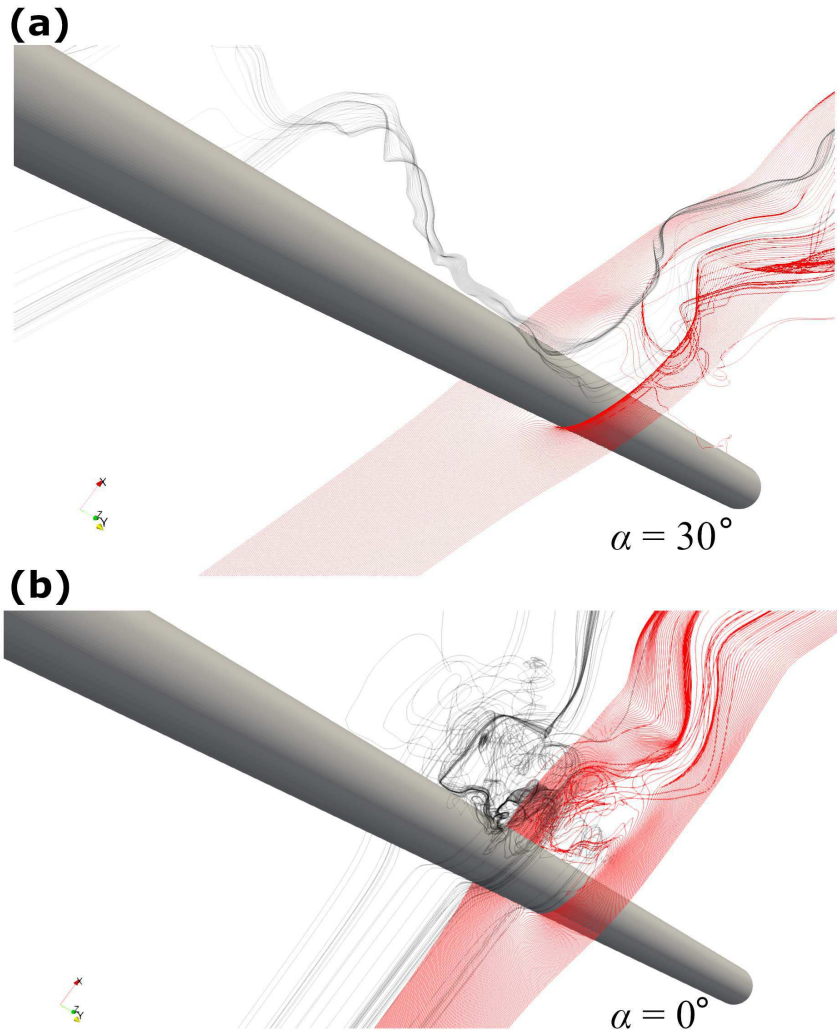

FIG. 11. Axial flow visualization at $Re = 10^4$ for the cases: (a) $\alpha = 30°$ and (b) $\alpha = 0°$. Axial flow tends to move along the center axis and interact with von Kármán vortices, a feature not observed in the normal flow case.

Accepted to Phys. Fluids 10.1063/5.0172648

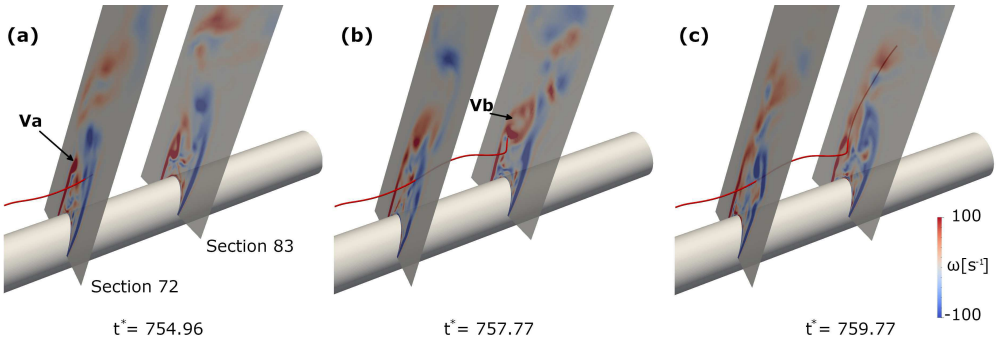

FIG. 12. Visualization of the interaction between axial and von Kármán vortices with a massless particle tracked by a red tube. Three time instances demonstrate the particles' movement through planes, and the evolving vortical structure, leading to a larger von Kármán vortex that eventually pulls the particle into the far wake.

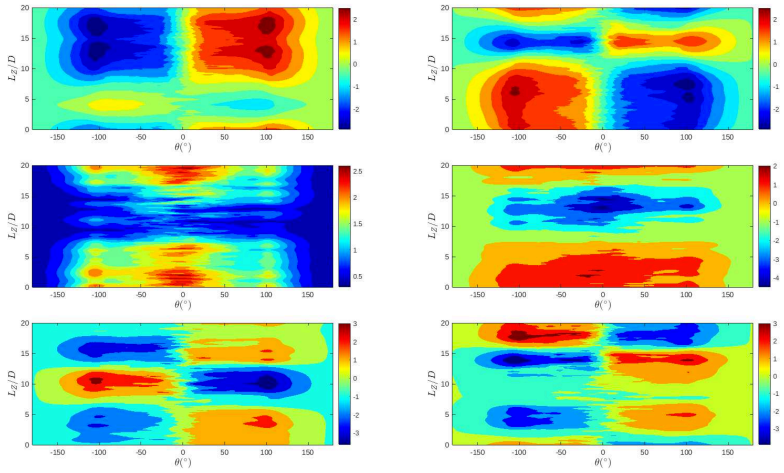

FIG. 13. The first six POD mode shapes for the surface pressure at $Re = 10^4$ and $\alpha = 0°$. The number of time sequence is 1800.

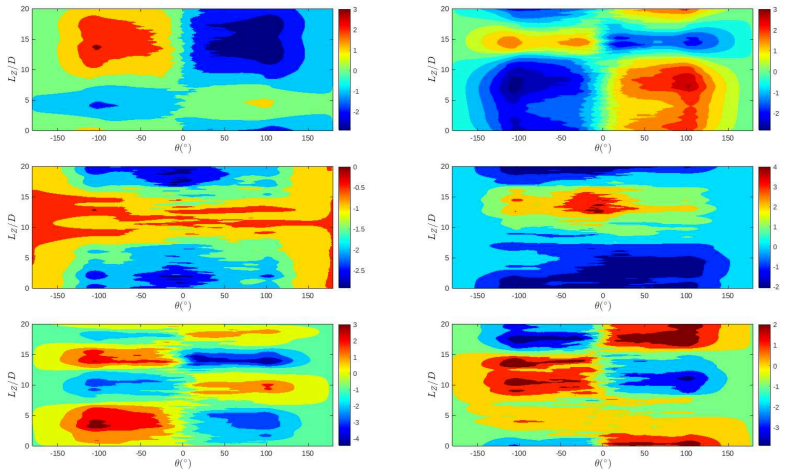

FIG. 14. The first six POD mode shapes for the surface pressure at $Re = 10^4$ and $\alpha = 0°$. The number of time sequence is 1200.

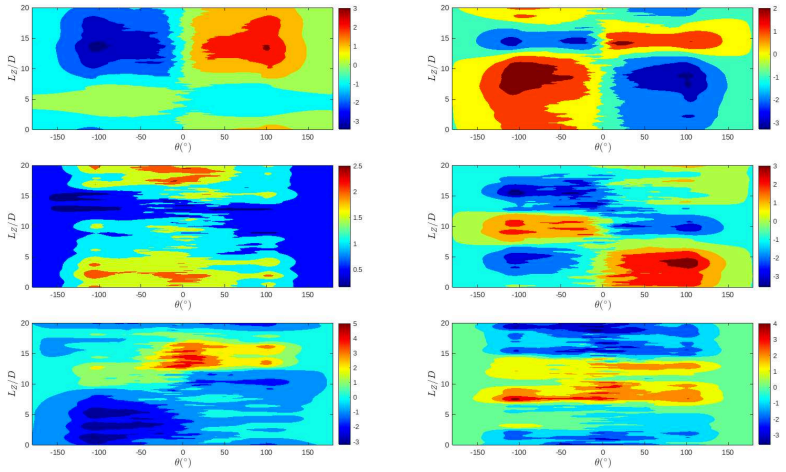

FIG. 15. The first six POD mode shapes for the surface pressure at $Re = 10^4$ and $\alpha = 0°$. The number of time sequence is 1000.

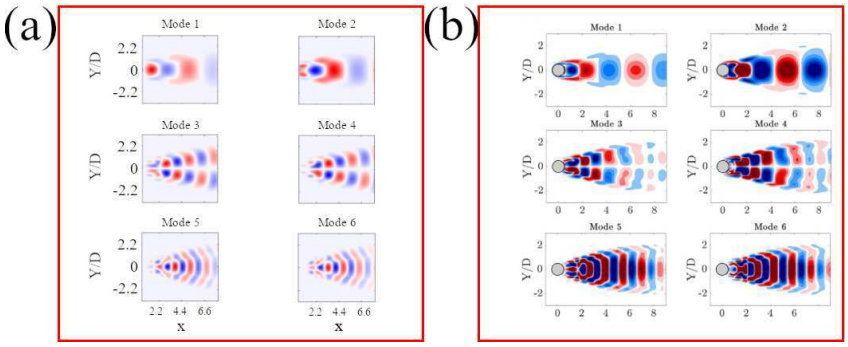

FIG. 16. A comparison of the mode shape for the span-vise vorticity at $Re = 100$: (a) current POD result (b) result from Janocha *et al.*[33].